Editors' Suggestion

Topological Phenomena in Artificial Quantum Materials Revealed by Local Chern Markers

Catalin D. Spataru,[1,*] Wei Pan,[1,†] and Alexander Cerjan[2,‡]
[1]*Sandia National Laboratories, Livermore, California 94551, USA*
[2]*Center for Integrated Nanotechnologies, Sandia National Laboratories, Albuquerque, New Mexico 87185, USA*

(Received 23 May 2024; revised 21 October 2024; accepted 24 February 2025; published 24 March 2025)

A striking example of frustration in physics is Hofstadter's butterfly, a fractal structure that emerges from the competition between a crystal's lattice periodicity and the magnetic length of an applied field. Current methods for predicting the topological invariants associated with Hofstadter's butterfly are challenging or impossible to apply to a range of materials, including those that are disordered or lack a bulk spectral gap. Here, we demonstrate a framework for predicting a material's local Chern markers using its position-space description and validate it against experimental observations of quantum transport in artificial graphene in a semiconductor heterostructure, inherently accounting for fabrication disorder strong enough to close the bulk spectral gap. By resolving local changes in the system's topology, we reveal the topological origins of antidot-localized states that appear in artificial graphene in the presence of a magnetic field. Moreover, we show the breadth of this framework by simulating how Hofstadter's butterfly emerges from an initially unpatterned 2D electron gas as the system's potential strength is increased and predict that artificial graphene becomes a topological insulator at the critical magnetic field. Overall, we anticipate that a position-space approach to determine a material's Chern invariant without requiring prior knowledge of its occupied states or bulk spectral gaps will enable a broad array of fundamental inquiries and provide a novel route to material discovery, especially in metallic, aperiodic, and disordered systems.

DOI: 10.1103/PhysRevLett.134.126601

Over the last half-century, few physical systems have been studied as intently as two-dimensional electron gases subjected to a perpendicularly oriented magnetic field. By itself, this configuration yields the integer quantum Hall effect, whose defining feature is a quantized conductivity stemming from protected edge-localized transport channels [1–3]. However, when a periodic electrostatic potential is applied, the system becomes frustrated—the applied magnetic field B is attempting to drive the system to exhibit degenerate Landau levels, characterized by the magnetic length $l_B = \sqrt{\hbar/eB}$, while the periodic potential tries to force the system to exhibit extended Bloch modes, characterized by the lattice constant a. This competition results in each band being split into subbands separated by minigaps that form a fractal as a function of the applied magnetic field and Fermi energy, Hofstadter's butterfly [4]. The fractal structure for a spectrally isolated underlying band is periodic in Φ/Φ_0, where $\Phi = BA$ is the magnetic flux through a unit cell with area A and $\Phi_0 = h/e$ is the magnetic flux quantum. Hofstadter's butterfly has been observed in artificial quantum materials [5–7] and more recently in graphene superlattices [8–12].

[*]Contact author: cdspata@sandia.gov
[†]Contact author: wpan@sandia.gov
[‡]Contact author: awcerja@sandia.gov

Despite substantial progress in achieving system periodicities large enough to enter the parameter regime where Hofstadter's butterfly manifests, $\Phi \sim \Phi_0$, it remains a formidable challenge to predict the Chern numbers associated with each minigap in experimentally realizable systems. For low-energy models with limited degrees of freedom, there are a few different approaches to predicting a minigap's Chern number: via a Diophantine equation [13–17], Středa's formula [18], semiclassical analysis [19], bulk-boundary correspondence [20–22], or direct calculation using the occupied states [23–25]. However, these methods are impossible or impractical to apply to many experimental platforms, stymied either by prohibitively large computational costs in the absence of a low-energy description, the lack of a bulk spectral gap due to disorder, or the need for system-specific knowledge [17,26,27]. In such cases, the last resort is direct simulation of a system's quantum transport [28,29], requiring the specification of a device geometry and still yielding a costly computational endeavor for realistic systems. Moreover, such an approach will miss bulk-embedded phenomena that do not contribute to the chosen transport channels.

Here, we theoretically demonstrate and experimentally validate the spectral localizer framework [30–32] for predicting a quantum material's local Chern topology and associated boundary-localized states. Moreover, we show how the spectral localizer framework can be used to reveal distinct material topology at different length scales of multiscale systems. Using this framework in artificial graphene [33,34] subjected to an out-of-plane magnetic field and described by a continuum model without a low-energy approximation, we demonstrate quantitative agreement between the Chern marker and the experimentally observed Hall conductivity, while inherently accounting for fabrication disorder that is strong enough to remove the system's spectral gaps. Moreover, by spatially resolving local changes in the system's topology, we show that many of the pinned states that populate the gaps between the bulk Landau levels are topological, stemming from the distinct topology of the antidots relative to the unpatterned bulk for many magnetic field strengths. Taking advantage of the spectral localizer's ability to efficiently operate without a low-energy approximation, we numerically observe the formation of Hofstadter's butterfly from an unpatterned system. Finally, we predict the opening of a topological band gap in artificial graphene at the critical magnetic field due to long-range couplings, yielding a topological insulator at modest magnetic fields. Looking forward, we anticipate that the spectral localizer framework's application to realistic multiscale systems will both yield a novel approach to material classification and enable a broad array of fundamental inquiries, such as those into the formation of Hofstadter's butterfly in twisted materials [35–37], as well as aid in the search for materials that exhibit the quantum anomalous Hall effect [38–45].

To motivate the development of our theoretical approach, we consider an electron gas confined to an effectively 2D quantum well layer in InAs surrounded by barrier layers of AlSb in a semiconductor heterostructure, into which an antidot triangular lattice is added via interferometric lithography. The triangular antidot lattice confines the electron gas in plane to areas furthest from the antidots yielding an effective honeycomb lattice for the electrons in the low-potential regions between three antidots coupled together via the potential troughs between two antidots [Figs. 1(a) and 1(b)], altogether creating artificial graphene. It has been shown [33,34,46–49] that the low-energy electronic band structure of artificial graphene mimics the behavior of natural graphene's Dirac cones. In the presence of a perpendicular, static magnetic field $\mathbf{B} = B\hat{\mathbf{z}}$, the 2D electron gas in artificial graphene is assumed to be noninteracting and characterized by the single-particle Hamiltonian

$$H = \frac{1}{2m^*}(-i\hbar\nabla + e\mathbf{A}(\mathbf{x}))^2 + V(\mathbf{x}) - \frac{\mu_B g}{\hbar} s_z B, \quad (1)$$

where the electrons have effective mass $m^* = m_{\mathrm{eff}} m_0$, $V(\mathbf{x})$ is a scalar potential that accounts for the system's nanoscale structure, and the strength of the Zeeman splitting is proportional to the effective Landé g factor of the heterostructure and the electron's spin s_z.

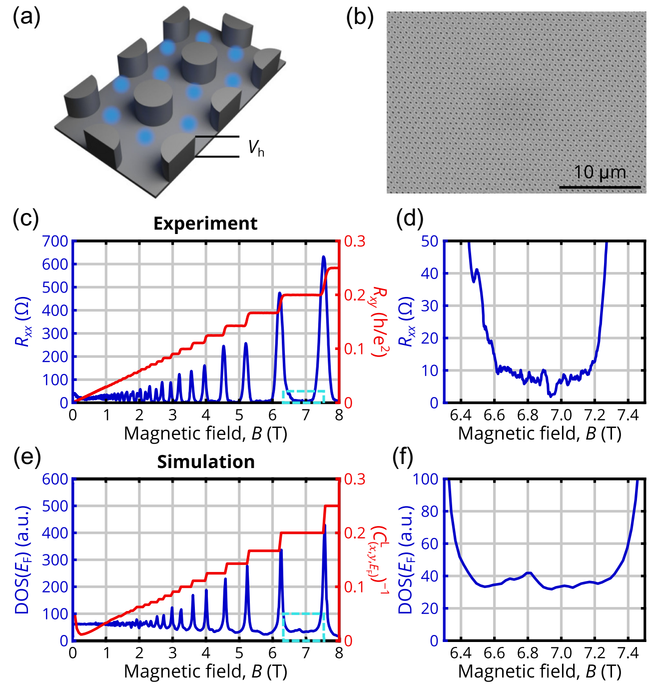

FIG. 1. (a) Schematic of the antidot potential profile (gray) with strength V_{h} and locations where the electrons are approximately localized (blue) to form the artificial graphene pseudo-atoms. (b) SEM image of a representative experimental specimen. (c) Measured longitudinal R_{xx} (blue) and transverse R_{xy} (red) resistances versus the magnetic field in the artificial graphene AlSb-InAs-AlSb semiconductor heterostructure at 0.3 with lattice constant $a = 250$ nm, antidot diameter $a/2$, and electron density $n \sim 8 \times 10^{11}$ cm^{-2}. (d) Enlarged view of the measured R_{xx} in the dashed cyan box in (c). (e) Calculated density of states (blue) and $(C^{\mathrm{L}}_{(x,y,E_{\mathrm{F}})})^{-1}$ calculated in the unpatterned bulk versus the applied magnetic field at the Fermi energy $E_{\mathrm{F}} = 85$ meV for artificial graphene with the same geometry as the experimental system with simulation flake size $\sim 2 \times 3.4$ μm^2, and model parameters $V_h = 25$ meV, normally distributed disorder with standard deviation $\delta V_{\mathrm{h}} = 5$ meV per antidot, $m^* = 0.023 m_0$, $g = 40$, and discretization $\Delta x = 2$ nm. $(C^{\mathrm{L}}_{(x,y,E_{\mathrm{F}})})^{-1}$ simulations use $\kappa = 1 \times 10^{-3}$ meV/nm. (f) Enlarged view of the simulated DOS(E_{F}) in the dashed cyan box in (e).

The measured longitudinal (R_{xx}) and Hall (R_{xy}) resistivities of our AlSb-InAs-AlSb artificial graphene heterostructure are shown in Figs. 1(c) and 1(d). Overall, the R_{xx} and R_{xy} traces resemble those of a typical 2D electron gas in an unpatterned heterostructure. Shubnikov–de Haas (SdH) oscillations are observed at low magnetic field strengths, and a fast Fourier transform analysis of these SdH oscillations yields an electron density of $n \sim 8 \times 10^{11}$ cm^{-2}. In the high B-field regime, fully developed quantized Hall states are formed, with R_{xx} assuming a low resistance value and R_{xy} quantized to the value of $h/e^2\nu$ in between Landau levels with filling factor $\nu = nh/eB$.

To numerically model artificial graphene using a position-space description, we first consider the zero-field limit of Eq. (1) and approximate the Laplacian in the kinetic term $K = -(\hbar^2/2m^*)\nabla^2$ using finite-difference (FD) methods [50] with vertex spacings $\Delta x = \Delta y$. This procedure transforms K into a sparse bounded matrix $K^{(\mathrm{FD})}$ in which adjacent vertices in the square lattice are coupled together with strength $t^{(\mathrm{FD})} = \hbar^2/(2m^*\Delta x^2)$. For electron energies E sufficiently smaller than $t^{(\mathrm{FD})}$, $K^{(\mathrm{FD})}$ accurately describes a free electron. When discretized, the potential energy $V(\mathbf{x})$ becomes a diagonal matrix $V^{(\mathrm{FD})}$ representing the potential strength at each vertex. Finally, the magnetic field is reintroduced both by using the Peierls substitution [51] in $K^{(\mathrm{FD})}$ (see Supplemental Material Sec. SI [52]), yielding a B-dependent phase to some of the couplings $t^{(\mathrm{FD})}$, and by including the Zeeman splitting in $V^{(\mathrm{FD})}$. Our model is parametrized by comparing R_{xx} against the density of states (DOS) of the discretized system [Figs. 1(e) and 1(f)], finding a Fermi level $E_\mathrm{F} \equiv \pi n \hbar^2/m^* \sim 85$ meV, and $g = 40$ using a uniform Zeeman splitting approximation [53,54].

However, in contrast to a free 2D electron gas, careful examination of R_{xx} in Figs. 1(c) and 1(d) shows additional features in between the system's main Landau levels, e.g., near $B = 7$ T. These features are numerically reproduced by choosing a disordered antidot potential strength $V_\mathrm{h} + \delta V_\mathrm{h}\xi$, with $V_\mathrm{h} = 25$ meV, $\delta V_\mathrm{h} = 5$ meV, and normally distributed ξ. Simulations show that the between-Landau level features correspond to states at the Fermi energy pinned to the antidots (Fig. 2) whose fine features in the ordered DOS are blurred out by disorder (see Supplemental Material Sec. SII [52]). As such, the difference in the relative prominence of these features in the observed R_{xx} versus the simulated DOS can be understood as these states' spatial pinning limiting their charge mobility and thus limiting their contribution to R_{xx} [66,67]. Experimentally, we also see that these pinned states have a vanishing contribution to the Hall conductance. Yet, as these antidot-localized states completely fill the bulk spectral gap, they prohibit the use of many approaches for predicting the Hall conductivity.

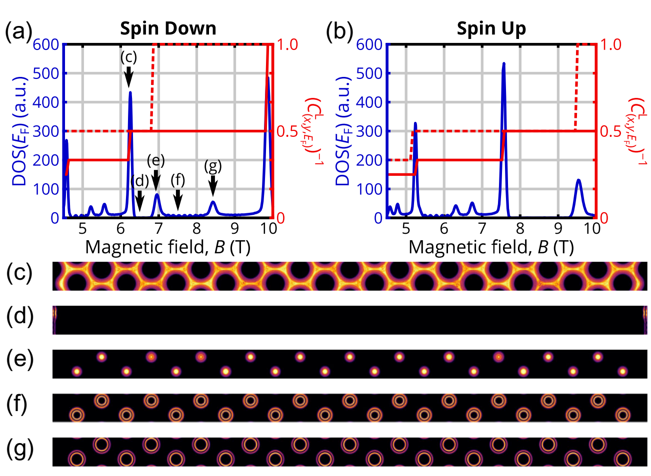

FIG. 2. (a),(b) Calculated DOS (blue) and local Chern marker inverse (red) for an ordered version of the system considered in Fig. 1, separated by spin. The local Chern marker is calculated both in the unpatterned bulk (solid) and center of an antidot (dashed) using $\kappa = 0.5$ meV/nm. (c)–(g) LDOS of the spin down sector at E_F showing bulk Landau levels at $B = 6.21$ T (c), chiral edge states at $B = 6.49$ T (d), antidot-localized Landau levels at $B = 6.94$ T (e), and chiral antidot–bulk interface-localized states at $B = 7.52$ T (f) and $B = 8.42$ T (g).

Instead, to predict the Chern invariants between the Landau levels of disordered artificial graphene despite the lack of a spectral gap at the Fermi energy, we employ the spectral localizer framework [30–32] that has previously been successful at classifying the topology of gapless acoustic metamaterials [68], photonic crystals [55,56], and toy models [69]. The spectral localizer is a composite operator formed by combining the eigenvalue equations of a finite system's Hamiltonian and position operators using a Clifford representation; in 2D, the Pauli matrices can be used, yielding

$$L_{(x,y,E)}(X,Y,H) = \kappa(X - x\mathbf{1}) \otimes \sigma_x + \kappa(Y - y\mathbf{1}) \otimes \sigma_y + (H - E\mathbf{1}) \otimes \sigma_z. \quad (2)$$

Here, X and Y are position operators, 1 is the identity, and $\kappa > 0$ is a scaling coefficient that ensures consistent units and similar spectral weighting between the summands. Heuristically, the choice of κ is analogous to the choice of integration region necessary for other local Chern markers [24,25]. The approximate scale of κ is set by the smallest dimension of the finite system L_min and the width of the relevant bulk spectral gap E_gap, as $\kappa \sim E_\mathrm{gap}/L_\mathrm{min}$ [57]. For artificial graphene in the absence of electron interactions, the Landau level spacing sets the size of the spectral gap, $E_\mathrm{gap}(B) = \hbar\omega_\mathrm{c}(B)$ where $\omega_\mathrm{c}(B)$ is the cyclotron frequency. In practice, choices of κ spanning many orders of magnitude provide quantitatively similar results (see Supplemental Material Sec. SIII [52]), though increasingly large simulation domains are needed for weak magnetic fields as $E_\mathrm{gap}(B)$ decreases.

The 2D spectral localizer defines a local Chern marker

$$C^\mathrm{L}_{(x,y,E)}(X,Y,H) = \frac{1}{2}\mathrm{sig}[L_{(x,y,E)}(X,Y,H)] \in \mathbb{Z}, \quad (3)$$

where sig denotes the matrix's signature, its number of positive eigenvalues minus its number of negative ones [30–32]. Heuristically, the ability of Eqs. (2) and (3) to predict a system's Hall conductivity can be understood as follows: First, for a given choice of (x, y, E), the spectral localizer is performing dimensional reduction from 2D to 0D, i.e., $L_{(x,y,E)}$ can be viewed as the Hamiltonian of a fictitious 0D system. Then, $C^\mathrm{L}_{(x,y,E)}$ is calculating the 0th Chern number of this fictitious 0D system. Finally, because the dimensional reduction is consistent with Bott

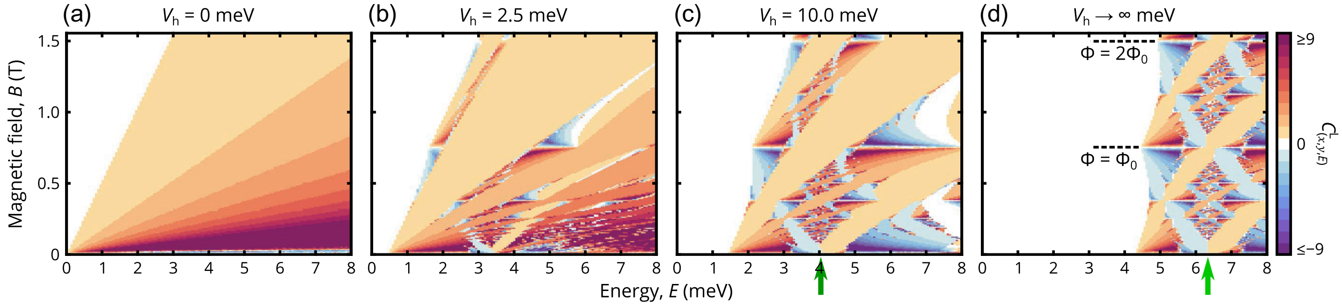

FIG. 3. (a)–(d) Predicted $C^{L}_{(x,y,E)}$ in the unpatterned bulk for a single spin sector as a function of magnetic field strength and energy for ordered artificial graphene with lattice constant $a = 80$ nm, antidot diameter $a/2$, $m^* = 0.030m_0$, $g = 0$. The flake size is $\sim 2 \times 2.2\ \mu\mathrm{m}^2$, with $\Delta x = 2$ nm and $\kappa = 4 \times 10^{-5}$ meV/nm. The potential strength is increased from $V_h = 0$ meV (a) to 2.5 (b), 10 (c), and ∞ meV (d). Green arrows denote the Dirac point energy at $B = 0$ T (see Supplemental Material Sec. SIV [52]).

periodicity [70], $C^{L}_{(x,y,E)}$ is equivalent to a local first Chern marker of the original 2D system at (x, y, E). For an infinite, gapped system with E in the relevant band gap, $C^{L}_{(x,y,E)}$ is provably equal to the first Chern number; in the thermodynamic limit the local Chern marker is defined through the spectral flow of $L_{(x,y,E)}$ [32,58].

Choosing (x, y, E_F) in the unpatterned bulk and at the Fermi energy, we find quantitative agreement between the measured R_{xy} and simulated $(C^{L}_{(x,y,E_F)})^{-1}$ of a system with disordered antidots, despite the lack of a spectral gap at the Fermi energy at every magnetic field strength [Figs. 1(c) and 1(e)]. However, by choosing (x, y, E_F) within an antidot and increasing $\kappa \sim 2E_{\mathrm{gap}}/a$ to resolve phenomena at a smaller spatial scale corresponding to the antidot diameter $a/2$ (see Supplemental Material Sec. SIII [52]), the local Chern marker reveals the topological origin of many of the antidot-pinned states. In particular, noting that $E_F > V_h$, the spectral localizer framework identifies that, in an ordered system at large magnetic fields, pinned states can both form highly degenerate antidot-confined Landau levels across which the local Chern marker changes its value independent from the marker evaluated in the unpatterned bulk, as well as chiral states localized to the interface between the antidot and the unpatterned bulk when the two regions have different local Chern numbers (Fig. 2). The distinction between these two types of pinned states can be seen in their local density of states (LDOS), see Figs. 2(e)–2(g), and their localization confirms why neither type of pinned state strongly contributes to the experimentally accessible R_{xx} and R_{xy}. When the local topology of the antidot regions matches that of the unpatterned bulk, the LDOS reveals those edge conduction channels responsible for R_{xy}, see Fig. 2(d); note, combining both spin sectors and adding disorder removes these B-field ranges where only chiral edge states exist to recover the DOS of Figs. 1(c)–1(f).

The ability to predict an experimental system's minigap Chern markers without needing to find its spectral gaps and occupied states, develop a V_h-customized effective model, or specify a transport geometry, offers a variety of possibilities. In Figs. 3(a)–3(d), we explore the emergence of Hofstadter's butterfly for a honeycomb lattice from an unpatterned 2D electron gas as the artificial graphene antidot potential strength is increased. In particular, by using a discretized version of the continuum Hamiltonian that automatically incorporates higher-energy phenomena, the spectral localizer framework can inherently consider the zero potential limit. As can be seen, for any positive potential strength, horizontal line segments with vanishing Chern markers, and about which the Chern marker changes sign, immediately appear for $\Phi/\Phi_0 \in \mathbb{Z}$. In the limit of $V_h \to \infty$ meV, Hofstadter's butterfly becomes nearly periodic about these lines as expected. These horizontal lines also persist at much larger E_F than the energy of the Dirac point, potentially aiding in experimental design (see Supplemental Material Sec. SV [52]). Additionally, our simulations also reveal how the minigaps in artificial graphene close and reopen as the antidot potential strength is increased so that the Chern invariant can change; for example, showing how the $C^L = -1$ minigap forms at the Dirac point in artificial graphene's low-energy bands at $B = 0$ T and slowly supersedes the $C^L \geq 2$ minigaps as V_h increases.

One of the characteristic features of graphene subjected to a magnetic field is the manifestation of the unconventional quantum Hall effect for Fermi energies near the Dirac point [71–75]. For sufficiently small B, this unconventional behavior is distinguished by a Landau level energy spacing following $E_j = v_g\sqrt{2e\hbar B|j|}$ with level index $j \in \mathbb{Z}$ and group velocity $v_g \approx h/(3m^* a)$ in the vicinity of the Dirac point [33]. Moreover, the Chern marker changes by 2 per spin across each such Landau level. For weak magnetic field strengths $B \gtrsim 0$ T, the spectral localizer framework reproduces this behavior for artificial graphene, identifying that the Chern marker changes by 2 per spin in the unconventional regime and the Landau level spacing is proportional to $\sqrt{|j|}$ [Figs. 4(a) and 4(b) and Supplemental Material Sec. SVI [52]]. Given the periodicity of Hofstadter's butterfly, the spectral localizer framework also

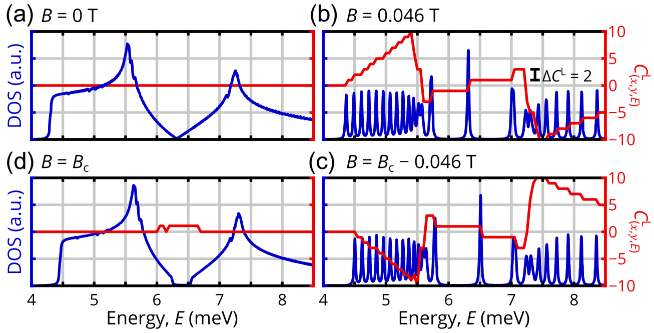

FIG. 4. (a)–(d) Density of states (blue) and $C^{\mathrm{L}}_{(x,y,E)}$ in the unpatterned bulk (red) for a single spin sector of artificial graphene with $V_{\mathrm{h}} \to \infty$meV using the same simulation parameters as Fig. 3 for magnetic field strengths near $B \sim 0$ T and the critical field $B \sim B_{\mathrm{c}}$ where $\Phi = \Phi_0$.

predicts the reappearance of the unconventional quantum Hall effect near B_{c} where $\Phi = \Phi_0$, with similar Landau level spacing but the opposite Hall conductivities for $B \lesssim B_{\mathrm{c}}$ [Figs. 4(c) and 4(d) and Supplemental Material Sec. SVI [52]].

For a honeycomb lattice with only nearest neighbor (NN) couplings, Hofstadter's butterfly is perfectly periodic at $B = B_{\mathrm{c}}$ where its DOS returns to that at $B = 0$ T. However, artificial graphene exhibits longer-range couplings between its pseudo-atoms as well whose effects are automatically incorporated through the use of a discretized continuum model; the approximate strength $t_{\mathrm{NNN}}/t_{\mathrm{NN}} \approx 0.13$ of the next-nearest neighbor (NNN) couplings can be estimated from the degree of chiral symmetry breaking in the $B = 0$ T band structure (see Supplemental Material Sec. SVI [52]). In the presence of a magnetic field, longer-range couplings alter the structure of Hofstadter's butterfly [76], and in artificial graphene they open a spectral gap around the $B = 0$ T Dirac point that the spectral localizer predicts is topological $C^{\mathrm{L}}_{(x,y,E)} = 1$ [Fig. 4(d)]. Thus, through careful control over the magnetic field in artificial graphene whose unit cell is large enough to yield experimentally accessible B_{c}, the spectral localizer framework shows that artificial graphene can become a topological insulator, offering opportunities for device applications [77].

In conclusion, we have demonstrated how the spectral localizer framework can identify the topological origins of artificial graphene's antidot-localized states, shown the emergence of Hofstadter's butterfly across both the zero- and strong-potential limits, and predicted that artificial graphene becomes a topological insulator at B_{c}. A sample implementation of the spectral localizer is provided as part of the Supplemental Material [52,78]. Overall, the spectral localizer framework possesses three key advantages: it can be applied directly to a material's single-particle position-space description without requiring a low-energy approximation, it can be applied without needing to find a system's occupied states or ensure the system has a bulk spectral gap at the Fermi energy, and it can reveal phenomena at different length scales of multiscale systems. Looking forward, we expect that the spectral localizer framework can be applied to any weakly correlated material, including metallic and aperiodic materials, and thus offers an entirely distinct approach to topological material classification than existing methods that are based on a material's band structure [79].

Acknowledgments—We thank Terry A. Loring, Sachin Vaidya, and Joseph J. Cuozzo for helpful discussions. The authors acknowledge support from the Laboratory Directed Research and Development program at Sandia National Laboratories. This work was performed, in part, at the Center for Integrated Nanotechnologies, an Office of Science User Facility operated for the U.S. Department of Energy (DOE) Office of Science. Sandia National Laboratories is a multimission laboratory managed and operated by National Technology and Engineering Solutions of Sandia, LLC, a wholly owned subsidiary of Honeywell International, Inc., for the U.S. DOE's National Nuclear Security Administration under Contract No. DE-NA-0003525.

[1] K. v. Klitzing, G. Dorda, and M. Pepper, New method for high-accuracy determination of the fine-structure constant based on quantized Hall resistance, Phys. Rev. Lett. **45**, 494 (1980).
[2] R. B. Laughlin, Quantized Hall conductivity in two dimensions, Phys. Rev. B **23**, 5632 (1981).
[3] B. I. Halperin, Quantized Hall conductance, current-carrying edge states, and the existence of extended states in a two-dimensional disordered potential, Phys. Rev. B **25**, 2185 (1982).
[4] Douglas R. Hofstadter, Energy levels and wave functions of Bloch electrons in rational and irrational magnetic fields, Phys. Rev. B **14**, 2239 (1976).
[5] Till Schlösser, Klaus Ensslin, Jörg P. Kotthaus, and Martin Holland, Landau subbands generated by a lateral electrostatic superlattice—chasing the Hofstadter butterfly, Semicond. Sci. Technol. **11**, 1582 (1996).
[6] C. Albrecht, J. H. Smet, K. von Klitzing, D. Weiss, V. Umansky, and H. Schweizer, Evidence of Hofstadter's fractal energy spectrum in the quantized Hall conductance, Phys. Rev. Lett. **86**, 147 (2001).
[7] M. C. Geisler, J. H. Smet, V. Umansky, K. von Klitzing, B. Naundorf, R. Ketzmerick, and H. Schweizer, Detection of a Landau band-coupling-induced rearrangement of the Hofstadter Butterfly, Phys. Rev. Lett. **92**, 256801 (2004).
[8] C. R. Dean, L. Wang, P. Maher, C. Forsythe, F. Ghahari, Y. Gao, J. Katoch, M. Ishigami, P. Moon, M. Koshino, T. Taniguchi, K. Watanabe, K. L. Shepard, J. Hone, and P. Kim, Hofstadter's butterfly and the fractal quantum Hall

effect in moiré superlattices, Nature (London) **497**, 598 (2013).

[9] B. Hunt, J. D. Sanchez-Yamagishi, A. F. Young, M. Yankowitz, B. J. LeRoy, K. Watanabe, T. Taniguchi, P. Moon, M. Koshino, P. Jarillo-Herrero, and R. C. Ashoori, Massive Dirac fermions and Hofstadter Butterfly in a van der Waals heterostructure, Science **340**, 1427 (2013).

[10] L. A. Ponomarenko, R. V. Gorbachev, G. L. Yu, D. C. Elias, R. Jalil, A. A. Patel, A. Mishchenko, A. S. Mayorov, C. R. Woods, J. R. Wallbank, M. Mucha-Kruczynski, B. A. Piot, M. Potemski, I. V. Grigorieva, K. S. Novoselov, F. Guinea, V. I. Fal'ko, and A. K. Geim, Cloning of Dirac fermions in graphene superlattices, Nature (London) **497**, 594 (2013).

[11] Carlos Forsythe, Xiaodong Zhou, Kenji Watanabe, Takashi Taniguchi, Abhay Pasupathy, Pilkyung Moon, Mikito Koshino, Philip Kim, and Cory R. Dean, Band structure engineering of 2D materials using patterned dielectric superlattices, Nat. Nanotechnol. **13**, 566 (2018).

[12] Xiaobo Lu, Biao Lian, Gaurav Chaudhary, Benjamin A. Piot, Giulio Romagnoli, Kenji Watanabe, Takashi Taniguchi, Martino Poggio, Allan H. MacDonald, B. Andrei Bernevig, and Dmitri K. Efetov, Multiple flat bands and topological Hofstadter butterfly in twisted bilayer graphene close to the second magic angle, Proc. Natl. Acad. Sci. U.S.A. **118**, e2100006118 (2021).

[13] G. H. Wannier, A result not dependent on rationality for Bloch electrons in a magnetic field, Phys. Status Solidi B **88**, 757 (1978).

[14] A. H. MacDonald, Quantized Hall effect in a hexagonal periodic potential, Phys. Rev. B **29**, 3057 (1984).

[15] I. Dana, Y. Avron, and J. Zak, Quantised Hall conductance in a perfect crystal, J. Phys. C **18**, L679 (1985).

[16] Masatoshi Sato, Daijiro Tobe, and Mahito Kohmoto, Hall conductance, topological quantum phase transition, and the Diophantine equation on the honeycomb lattice, Phys. Rev. B **78**, 235322 (2008).

[17] J. E. Avron, O. Kenneth, and G. Yehoshua, A study of the ambiguity in the solutions to the Diophantine equation for Chern numbers, J. Phys. A **47**, 185202 (2014).

[18] P. Středa, Quantised Hall effect in a two-dimensional periodic potential, J. Phys. C **15**, L1299 (1982).

[19] Ming-Che Chang and Qian Niu, Berry phase, hyperorbits, and the Hofstadter spectrum: Semiclassical dynamics in magnetic Bloch bands, Phys. Rev. B **53**, 7010 (1996).

[20] Yasuhiro Hatsugai, Takahiro Fukui, and Hideo Aoki, Topological analysis of the quantum Hall effect in graphene: Dirac-Fermi transition across van Hove singularities and edge versus bulk quantum numbers, Phys. Rev. B **74**, 205414 (2006).

[21] Julio Cesar Avila, Hermann Schulz-Baldes, and Carlos Villegas-Blas, Topological invariants of edge states for periodic two-dimensional models, Math. Phys. Anal. Geom. **16**, 137 (2013).

[22] A. Agazzi, J.-P. Eckmann, and G. M. Graf, The colored Hofstadter butterfly for the Honeycomb lattice, J. Stat. Phys. **156**, 417 (2014).

[23] D. J. Thouless, M. Kohmoto, M. P. Nightingale, and M. den Nijs, Quantized Hall conductance in a two-dimensional periodic potential, Phys. Rev. Lett. **49**, 405 (1982).

[24] Alexei Kitaev, Anyons in an exactly solved model and beyond, Ann. Phys. (Amsterdam) **321**, 2 (2006).

[25] Raffaello Bianco and Raffaele Resta, Mapping topological order in coordinate space, Phys. Rev. B **84**, 241106(R) (2011).

[26] Biao Lian, Fang Xie, and B. A. Bernevig, Open momentum space method for the Hofstadter butterfly and the quantized Lorentz susceptibility, Phys. Rev. B **103**, L161405 (2021).

[27] S. Janecek, M. Aichinger, and E. R. Hernández, Two-dimensional Bloch electrons in perpendicular magnetic fields: An exact calculation of the Hofstadter butterfly spectrum, Phys. Rev. B **87**, 235429 (2013).

[28] Christoph W. Groth, Michael Wimmer, Anton R. Akhmerov, and Xavier Waintal, Kwant: A software package for quantum transport, New J. Phys. **16**, 063065 (2014).

[29] Santiago Giménez de Castro, João M. Viana Parente Lopes, Aires Ferreira, and D. A. Bahamon, Fast Fourier-Chebyshev approach to real-space simulations of the Kubo formula, Phys. Rev. Lett. **132**, 076302 (2024).

[30] Terry A Loring, K-theory and pseudospectra for topological insulators, Ann. Phys. (Amsterdam) **356**, 383 (2015).

[31] Terry A. Loring and Hermann Schulz-Baldes, Finite volume calculation of K-theory invariants, N. Y. J. Math. **23**, 1111 (2017), http://nyjm.albany.edu/j/2017/23-48.html.

[32] Terry A. Loring and Hermann Schulz-Baldes, The spectral localizer for even index pairings, J. Noncommut. Geom. **14**, 1 (2020).

[33] Cheol-Hwan Park, Young-Woo Son, Li Yang, Marvin L. Cohen, and Steven G. Louie, Electron beam supercollimation in graphene superlattices, Nano Lett. **8**, 2920 (2008).

[34] B. Wunsch, F. Guinea, and F. Sols, Dirac-point engineering and topological phase transitions in honeycomb optical lattices, New J. Phys. **10**, 103027 (2008).

[35] R. Bistritzer and A. H. MacDonald, Moiré butterflies in twisted bilayer graphene, Phys. Rev. B **84**, 035440 (2011).

[36] Kasra Hejazi, Chunxiao Liu, and Leon Balents, Landau levels in twisted bilayer graphene and semiclassical orbits, Phys. Rev. B **100**, 035115 (2019).

[37] Ya-Hui Zhang, Hoi Chun Po, and T. Senthil, Landau level degeneracy in twisted bilayer graphene: Role of symmetry breaking, Phys. Rev. B **100**, 125104 (2019).

[38] Naoto Nagaosa, Jairo Sinova, Shigeki Onoda, A. H. MacDonald, and N. P. Ong, Anomalous Hall effect, Rev. Mod. Phys. **82**, 1539 (2010).

[39] Cui-Zu Chang *et al.*, Experimental observation of the quantum anomalous Hall effect in a magnetic topological insulator, Science **340**, 167 (2013).

[40] Aaron L. Sharpe, Eli J. Fox, Arthur W. Barnard, Joe Finney, Kenji Watanabe, Takashi Taniguchi, M. A. Kastner, and David Goldhaber-Gordon, Emergent ferromagnetism near three-quarters filling in twisted bilayer graphene, Science **365**, 605 (2019).

[41] Yujun Deng, Yijun Yu, Meng Zhu Shi, Zhongxun Guo, Zihan Xu, Jing Wang, Xian Hui Chen, and Yuanbo Zhang, Quantum anomalous Hall effect in intrinsic magnetic topological insulator MnBi2Te4, Science **367**, 895 (2020).

[42] M. Serlin, C. L. Tschirhart, H. Polshyn, Y. Zhang, J. Zhu, K. Watanabe, T. Taniguchi, L. Balents, and A. F. Young, Intrinsic quantized anomalous Hall effect in a moiré heterostructure, Science **367**, 900 (2020).

[43] Guorui Chen, Aaron L. Sharpe, Eli J. Fox, Ya-Hui Zhang, Shaoxin Wang, Lili Jiang, Bosai Lyu, Hongyuan Li, Kenji Watanabe, Takashi Taniguchi, Zhiwen Shi, T. Senthil, David Goldhaber-Gordon, Yuanbo Zhang, and Feng Wang, Tunable correlated Chern insulator and ferromagnetism in a moiré superlattice, Nature (London) **579**, 56 (2020).

[44] Tingxin Li, Shengwei Jiang, Bowen Shen, Yang Zhang, Lizhong Li, Zui Tao, Trithep Devakul, Kenji Watanabe, Takashi Taniguchi, Liang Fu, Jie Shan, and Kin Fai Mak, Quantum anomalous Hall effect from intertwined moiré bands, Nature (London) **600**, 641 (2021).

[45] Wenjin Zhao, Kaifei Kang, Yichi Zhang, Patrick Knüppel, Zui Tao, Lizhong Li, Charles L. Tschirhart, Evgeny Redekop, Kenji Watanabe, Takashi Taniguchi, Andrea F. Young, Jie Shan, and Kin Fai Mak, Realization of the Haldane Chern insulator in a moiré lattice, Nat. Phys. **20**, 275 (2024).

[46] Sheng Wang, Diego Scarabelli, Lingjie Du, Yuliya Y. Kuznetsova, Loren N. Pfeiffer, Ken W. West, Geoff C. Gardner, Michael J. Manfra, Vittorio Pellegrini, Shalom J. Wind, and Aron Pinczuk, Observation of Dirac bands in artificial graphene in small-period nanopatterned GaAs quantum wells, Nat. Nanotechnol. **13**, 29 (2018).

[47] Lingjie Du, Sheng Wang, Diego Scarabelli, Loren N. Pfeiffer, Ken W. West, Saeed Fallahi, Geoff C. Gardner, Michael J. Manfra, Vittorio Pellegrini, Shalom J. Wind, and Aron Pinczuk, Emerging many-body effects in semiconductor artificial graphene with low disorder, Nat. Commun. **9**, 3299 (2018).

[48] Shu-guang Cheng, Jie Liu, Haiwen Liu, Hua Jiang, Qing-Feng Sun, and X. C. Xie, Majorana zero modes from topological kink states in the two-dimensional electron gas, Phys. Rev. B **101**, 165420 (2020).

[49] O. A. Tkachenko, V. A. Tkachenko, D. G. Baksheev, and O. P. Sushkov, Wannier diagrams for semiconductor artificial graphene, JETP Lett. **116**, 638 (2022).

[50] J. W. Thomas, *Numerical Partial Differential Equations: Finite Difference Methods*, 1st ed. (Springer, New York, Berlin Heidelberg, 1995).

[51] M. Graf and P. Vogl, Electromagnetic fields and dielectric response in empirical tight-binding theory, Phys. Rev. B **51**, 4940 (1995).

[52] See Supplemental Material at http://link.aps.org/supplemental/10.1103/PhysRevLett.134.126601 for a discussion of the fabrication and numerical methods, demonstrations of the convergence of the numerical methods, and supporting simulations of Hofstadter's butterfly in both artificial graphene and tight-binding models, which includes Refs. [22,24,25,53–65].

[53] S. S. Krishtopenko, V. I. Gavrilenko, and M. Goiran, Theory of g-factor enhancement in narrow-gap quantum well heterostructures, J. Phys. Condens. Matter **23**, 385601 (2011).

[54] W. Pan, K. W. Baldwin, K. W. West, L. N. Pfeiffer, and D. C. Tsui, Quantitative examination of the collapse of spin splitting in the quantum Hall regime, Phys. Rev. B **84**, 161307(R) (2011).

[55] Alexander Cerjan and Terry A. Loring, An operator-based approach to topological photonics, Nanophotonics **11**, 4765 (2022).

[56] Kahlil Y. Dixon, Terry A. Loring, and Alexander Cerjan, Classifying topology in photonic heterostructures with gapless environments, Phys. Rev. Lett. **131**, 213801 (2023).

[57] A. Cerjan, T. A. Loring, and H. Schulz-Baldes, Local markers for crystalline topology, Phys. Rev. Lett. **132**, 073803 (2024).

[58] Alexander Cerjan and Terry A. Loring, Classifying photonic topology using the spectral localizer and numerical K-theory, APL Photonics **9**, 111102 (2024).

[59] J. J. Sylvester, XIX. A demonstration of the theorem that every homogeneous quadratic polynomial is reducible by real orthogonal substitutions to the form of a sum of positive and negative squares, Lond. Edinb. Dublin Phil. Mag. J. Sci. **4**, 138 (1852).

[60] Iain S. Duff, MA57—a code for the solution of sparse symmetric definite and indefinite systems, ACM Trans. Math. Softw. **30**, 118 (2004).

[61] Hermann Weyl, Das asymptotische Verteilungsgesetz der Eigenwerte linearer partieller Differentialgleichungen (mit einer Anwendung auf die Theorie der Hohlraumstrahlung), Math. Ann. **71**, 441 (1912).

[62] Rajendra Bhatia, *Matrix Analysis*, Graduate Texts in Mathematics Vol. 169 (Springer, New York, NY, 1997).

[63] Alexander Cerjan, Terry A. Loring, and Fredy Vides, Quadratic pseudospectrum for identifying localized states, J. Math. Phys. (N.Y.) **64**, 023501 (2023).

[64] Jacob Shapiro, *The Loring–Schulz-Baldes Spectral Localizaer Revisited* (American Mathematical Society, Providence, 2025).

[65] Wang Yao, Shengyuan A. Yang, and Qian Niu, Edge states in graphene: From gapped flat-band to gapless chiral modes, Phys. Rev. Lett. **102**, 096801 (2009).

[66] B. L. Altshuler, D. Khmel'nitzkii, A. I. Larkin, and P. A. Lee, Magnetoresistance and Hall effect in a disordered two-dimensional electron gas, Phys. Rev. B **22**, 5142 (1980).

[67] D. Weiss, M. L. Roukes, A. Menschig, P. Grambow, K. von Klitzing, and G. Weimann, Electron pinball and commensurate orbits in a periodic array of scatterers, Phys. Rev. Lett. **66**, 2790 (1991).

[68] Wenting Cheng, Alexander Cerjan, Ssu-Ying Chen, Emil Prodan, Terry A. Loring, and Camelia Prodan, Revealing topology in metals using experimental protocols inspired by K-theory, Nat. Commun. **14**, 3071 (2023).

[69] Alexander Cerjan and Terry A. Loring, Local invariants identify topology in metals and gapless systems, Phys. Rev. B **106**, 064109 (2022).

[70] Michael Stone, Ching-Kai Chiu, and Abhishek Roy, Symmetries, dimensions and topological insulators: The mechanism behind the face of the Bott clock, J. Phys. A **44**, 045001 (2010).

[71] Yisong Zheng and Tsuneya Ando, Hall conductivity of a two-dimensional graphite system, Phys. Rev. B **65**, 245420 (2002).

[72] V. P. Gusynin and S. G. Sharapov, Unconventional integer quantum Hall effect in graphene, Phys. Rev. Lett. **95**, 146801 (2005).

[73] Yuanbo Zhang, Yan-Wen Tan, Horst L. Stormer, and Philip Kim, Experimental observation of the quantum Hall effect

and Berry's phase in graphene, Nature (London) **438**, 201 (2005).

[74] K. S. Novoselov, A. K. Geim, S. V. Morozov, D. Jiang, M. I. Katsnelson, I. V. Grigorieva, S. V. Dubonos, and A. A. Firsov, Two-dimensional gas of massless Dirac fermions in graphene, Nature (London) **438**, 197 (2005).

[75] D. N. Sheng, L. Sheng, and Z. Y. Weng, Quantum Hall effect in graphene: Disorder effect and phase diagram, Phys. Rev. B **73**, 233406 (2006).

[76] Jing-Min Hou and Wen-Xing Yang, Next-nearest-neighbor-tunneling-induced symmetry breaking of Hofstadter's butterfly spectrum for ultracold atoms on the honeycomb lattice, Phys. Lett. A **373**, 2774 (2009).

[77] Kostya Novoselov, Mind the gap, Nat. Mater. **6**, 720 (2007).

[78] C. D. Spataru, sandialabs/code-for-electronic-and-topological-properties-of-artificial-graphene-, Sandia National Laboratories, 2025, https://github.com/sandialabs/code-for-electronic-and-topological-properties-of-artificial-graphene-.

[79] Barry Bradlyn, L. Elcoro, Jennifer Cano, M. G. Vergniory, Zhijun Wang, C. Felser, M. I. Aroyo, and B. Andrei Bernevig, Topological quantum chemistry, Nature (London) **547**, 298 (2017).